A numerical study of cryogenic fluid injection and mixing under supercritical conditions

Nan Zong
The Pennsylvania State University, 237 Research Building East, University Park, Pennsylvania 16802

Hua Meng
The Pennsylvania State University, USB1 Suite B, University Park, Pennsylvania 16802

Shih-Yang Hsieh
GE Aircraft Engine, One Neumann Road, Cincinnati, Ohio 45215

Vigor Yang[a)]
The Pennsylvania State University, 104 Research Building East, University Park, Pennsylvania 16802

(Received 9 March 2004; accepted 27 July 2004; published online 21 October 2004)

The evolution of a cryogenic fluid jet initially at a subcritical temperature and injected into a supercritical environment, in which both the pressure and temperature exceed the thermodynamic critical state, has been investigated numerically. The model accommodates full conservation laws and real-fluid thermodynamics and transport phenomena. All of the thermophysical properties are determined directly from fundamental thermodynamics theories, along with the use of the corresponding state principles. Turbulence closure is achieved using a large-eddy-simulation technique. As a specific example, the dynamics of a nitrogen fluid jet is studied systematically over a broad range of ambient pressure. Owing to the differences of fluid states and flow conditions between the jet and surroundings, a string of strong density-gradient regimes is generated around the jet surface and exerts a stabilizing effect on the flow development. The surface layer acts like a solid wall that transfers the turbulent kinetic energy from its axial to radial component. The spatial growth rate of the surface instability wave increases with increasing pressure. The frequency of the most unstable mode exhibits a weak pressure dependence at high pressures. It, however, decreases significantly in the near-critical regime due to the enhanced effect of density stratification and increased mixing-layer momentum thickness. The result agrees well with the linear stability analysis. The jet dynamics is largely dictated by the local thermodynamic state through its influence on the fluid thermophysical properties. When the fluid temperature transits across the inflection point on an isobaric density-temperature curve, the resultant rapid property variations may qualitatively modify the jet behavior compared with its counterpart at low pressures. An increase in the ambient pressure results in an earlier transition of the jet into the self-similar regime. © *2004 American Institute of Physics*. [DOI: 10.1063/1.1795011]

I. INTRODUCTION

Injection of liquid fluid initially at a subcritical temperature into an environment in which the temperature and pressure exceed the thermodynamic critical point of the injected fluid is an important phenomenon in many high-pressure combustion devices, including diesel, gas turbine, and liquid-propellant rocket engines. Under these conditions, fluid jets exhibit many characteristics distinct from their counterparts at low pressures. First, because of the diminishment of surface tension and enthalpy of vaporization, the sharp distinction between the liquid and gas phases vanishes. The fluid properties and their spatial gradients vary continuously throughout the entire field. Second, thermodynamic and transport anomalies may occur during the temperature transition across the critical value, especially when the pressure approaches the critical point, a phenomenon commonly referred to as near-critical enhancement.[1] As a result, compressibility effects (i.e., volumetric changes induced by pressure variations) and variable inertial effects (i.e., volumetric changes induced by heat addition and/or variable composition) play an important role in dictating the flow evolution. Third, the characteristic times of the flow motions around the jet boundary have the same order of magnitude at supercritical conditions. The resultant coupling dynamics becomes transient in both the jet interior and the surrounding fluid, and involves an array of physiochemical processes with widely disparate time and length scales. Fourth, the flow Reynolds number increases almost linearly with pressure. For oxygen and hydrogen, an increase in pressure from 1 to 100 atm results in a reduction of the corresponding kinematic viscosity by a factor of 2 orders of magnitude. Based on the Kolmogorov universal equilibrium theory, the Kolmogorov and Taylor microscales may decrease by 1.5 and 1.0 orders of magnitude, respectively. These reductions of characteristic scales of turbulent motions have a direct impact on the flow evolution and the numerical grid density

[a)]Author to whom correspondence should be addressed. Telephone: +1(814) 863-1502. Fax: +1(814) 865-4784. Electronic mail: vigor@psu.edu

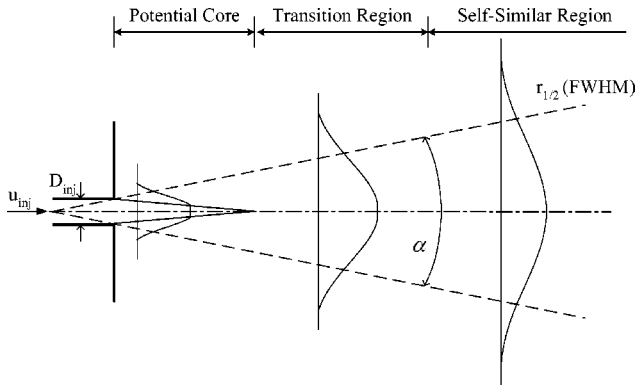

FIG. 1. Schematic of fluid jet evolution.

required to resolve key processes.[2] Comprehensive reviews of the state of knowledge on supercritical mixing and combustion were recently given by Yang[3] and Bellan.[4]

Substantial efforts have been applied to study fluid jets at low pressures in the past five decades. Three distinct flow regimes were commonly observed in a turbulent jet: a potential core, a transition region, and a fully developed self-similar region, as illustrated in Fig. 1. The potential core only contains the injected fluid and reduces in size as the jet mixes with the entrained ambient fluid. The flow properties along the centerline remain nearly constant in this region. Downstream of the potential core, there exists a transition region where turbulent mixing takes place. A fully developed self-similar region is reached further downstream, where the profiles of normalized flow properties collapse into single curves. For an incompressible gas jet, Schetz[5] stated that the self-similar region appears at approximately $x/D_{\mathrm{inj}} \geqslant 40$, whereas other studies[6] suggested a different location, as close as $x/D_{\mathrm{inj}} \geqslant 20$.

Experimental investigation into supercritical fluid jet dynamics dates back to 1971. Newman and Brzustowski[7] studied the injection of CO_2 fluid with an inlet temperature of 295 K into a chamber filled with CO_2 and N_2 mixtures under near critical conditions. The critical temperature and pressure of CO_2 are 304 K and 73 atm, respectively, and those of N_2 are 126 K and 34 atm, respectively. The chamber temperature and pressure were preconditioned in the range of 295–330 K and 62–90 atm, respectively, and the CO_2 mass fraction varied from 0% to 50%. The shadowgraph visualization technique was employed to investigate the jet flow evolution and its interaction with the surrounding fluid. Results indicated that over the pressure range considered, the jet surface structure and spray formation were suppressed with increasing temperature and CO_2 concentration in the chamber, mainly due to the diminished surface tension and enhanced CO_2 evaporation at near and above the critical temperature. Droplets were observed around the jet boundary, but their sizes decreased with an increase in the ambient temperature. The jet could be globally treated as a variable-density, single-phase turbulent submerged jet at both subcritical and supercritical pressures, when the ambient temperature remained supercritical.

Motivated by the development of high-pressure cryogenic-propellant rocket engines, extensive experimental studies have recently been conducted to provide direct insight into supercritical fluid injection and mixing. The work included injection of liquid nitrogen and coinjection of liquid nitrogen and gaseous helium into gaseous nitrogen environments over a wide range of pressure.[8–10] Cryogenic propellants such as liquid oxygen and hydrogen under both cold-flow and hot-fire test conditions were also considered. Results from the shadowgraph images confirmed the findings by Newman and Brzustowski.[7] Drastic changes in jet surface phenomena took place across the critical pressure. Ligaments and droplets formed at subcritical pressures, but disappeared at supercritical conditions due to the prevalence of turbulent motions and vanishing of surface tension. The jet surface topology bears a strong resemblance to its gaseous counterpart, with the spatial growth rate following that of an incompressible variable-density gaseous jet.[10] The spontaneous Raman scattering technique was employed to measure the density field.[11,12] In general, the normalized density profiles indicated a tendency towards the self-similarity solution observed for classical constant- and variable-density single-phase fluid jets at low pressures. The effects of acoustic waves on cryogenic nitrogen jet flow development were recently studied by Chehroudi *et al.*[13] The influence was substantial at subcritical conditions, but became unnoticeable at supercritical conditions. The phenomenon may be attributed to the formation of high-frequency vortices in the supercritical jet flow.

In parallel to experimental studies, attempts were made both theoretically and numerically to explore the underlying mechanisms of high-pressure fluid injection and mixing. Oefelein and Yang[2] modeled two-dimensional mixing and combustion of oxygen and hydrogen streams at supercritical conditions by means of a large-eddy-simulation technique. The formulation accommodated real-fluid thermodynamics and transport phenomena. All the thermophysical properties were evaluated directly from fundamental thermodynamics theories over the entire regime of fluid states of concern. Furthermore, a unified treatment of numerical algorithms based on general fluid thermodynamics was established to improve computational accuracy and efficiency.[3,14] Bellan and colleagues[15–17] treated the temporal evolution of heptane/nitrogen and oxygen/hydrogen mixing layers at supercritical conditions. Several important characteristics of high-pressure transitional mixing processes were identified. In particular, as a result of density stratification, the mixing layer is considerably more stable than a corresponding gaseous mixing layer. Energy dissipation due to both the species-flux and heat-flux effects prevails during the evolution of the mixing layer, whereas the viscous effect appears minimal.

The purpose of the present work is to conduct a comprehensive analysis of cryogenic fluid injection and mixing under supercritical conditions. The theoretical formulation accommodates full conservation laws and real-fluid thermodynamics and transport phenomena. Turbulence closure is achieved using a large-eddy-simulation technique. As a specific example, the dynamics of a cryogenic nitrogen jet in a supercritical nitrogen environment is studied over a wide

range of pressure. The work focuses on the near-field jet dynamics and its subsequent evolution.

II. THEORETICAL FORMULATION

A unified theoretical framework capable of treating fluid flows, transcritical property variations, and real-fluid thermodynamics is developed. Turbulence closure is achieved using a large-eddy-simulation technique, in which large-scale motions are calculated explicitly and the effects of unresolved small-scale turbulence are modeled either analytically or empirically. Thermodynamic properties such as enthalpy, Gibbs energy, and constant-pressure specific heat are obtained directly from fundamental thermodynamics.[3,14] Transport properties are evaluated using an extended corresponding-state theory along with the 32-term Benedict–Webb–Robin equation of state.[3]

A. Governing equations

The formulation is based on the Favre-filtered conservation equations of mass, momentum, and energy. These equations are derived by filtering the small-scale dynamics from the resolved scales over a well-defined set of spatial and temporal intervals. They can be conveniently expressed in the following Cartesian tensor form:

$$\frac{\partial \overline{\rho}}{\partial t} + \frac{\partial \overline{\rho}\widetilde{u}_j}{\partial x_j} = 0, \tag{1}$$

$$\frac{\partial \overline{\rho}\widetilde{u}_i}{\partial t} + \frac{\partial (\overline{\rho}\widetilde{u}_i\widetilde{u}_i + \overline{\rho}\delta_{ij})}{\partial x_j} = \frac{\partial (\overline{\tau}_{ij} - \tau_{ij}^{\mathrm{sgs}})}{\partial x_j}, \tag{2}$$

$$\frac{\partial \overline{\rho}\widetilde{E}}{\partial t} + \frac{\partial [(\overline{\rho}\widetilde{E} + \overline{\rho})\widetilde{u}_i]}{\partial x_i} = \frac{\partial}{\partial x_i}(\widetilde{u}_j\overline{\tau}_{ij} + \overline{q}_i - H_i^{\mathrm{sgs}} + \sigma_{ij}^{\mathrm{sgs}}), \tag{3}$$

where overbars and tildes denote resolved-scale and Favre-averaged resolved-scale variables, respectively. ρ, u_i, p, E, τ_{ij}, and q_i represent the density, velocity components, pressure, specific total energy, viscous stress tensor, heat flux, respectively. A detailed derivation of the filtered equations is presented by Oefelein and Yang.[2] The unclosed subgrid-scale (sgs) terms in Eqs. (1)–(3), including the stresses τ_{ij}^{sgs}, energy fluxes H_i^{sgs}, and viscous work $\sigma_{ij}^{\mathrm{sgs}}$, are defined as

$$\tau_{ij}^{\mathrm{sgs}} = (\overline{\rho u_i u_j} - \overline{\rho}\widetilde{u}_i\widetilde{u}_j), \tag{4}$$

$$H_i^{\mathrm{sgs}} = (\overline{\rho E u_i} - \overline{\rho}\widetilde{E}\widetilde{u}_i) + (\overline{\rho u}_i - \overline{\rho}\widetilde{u}_i), \tag{5}$$

$$\sigma_{ij}^{\mathrm{sgs}} = (\overline{u_j\tau_{ij}} - \widetilde{u}_j\widetilde{\tau}_{ij}). \tag{6}$$

The unclosed sgs stress term is modeled using the compressible flow version of the Smagorinsky model suggested by Erlebacher *et al.*[18]

$$\tau_{ij}^{sgs} = -2\nu_t\overline{\rho}(\widetilde{S}_{ij} - \widetilde{S}_{kk}\delta_{ij}/3) + \tfrac{2}{3}\overline{\rho}\overline{k}^{\mathrm{sgs}}\delta_{ij}, \tag{7}$$

where

$$\nu_t = C_R\Delta^2(2\widetilde{S}_{ij}\widetilde{S}_{ij})^{1/2}, \tag{8}$$

$$k^{\mathrm{sgs}} = C_I\Delta^2(2\widetilde{S}_{ij}\widetilde{S}_{ij}). \tag{9}$$

The dimensionless constants $C_R(\approx 0.01)$ and $C_I(\approx 0.007)$ are determined empirically, $k^{\mathrm{sgs}} = \tau_{kk}^{\mathrm{sgs}}/2\overline{\rho} = (\overline{\rho u_k u_k}/\overline{\rho} - \widetilde{u}_k\widetilde{u}_k)/2$ and $\widetilde{S}_{ij} = (\partial\widetilde{u}_i/\partial x_j + \partial\widetilde{u}_j/\partial x_i)/2$. The symbol Δ denotes the filter width. The subgrid energy flux term H_i^{sgs} is modeled as

$$H_i^{\mathrm{sgs}} = -\overline{\rho}\frac{\nu_t}{\mathrm{Pr}_t}\left(\frac{\partial\widetilde{h}}{\partial x_j} + \widetilde{u}_i\frac{\partial\widetilde{u}_i}{\partial x_j} + \frac{1}{2}\frac{\partial k^{\mathrm{sgs}}}{\partial x_j}\right). \tag{10}$$

A standard value of 0.7 is used for the turbulent Prandtl number. The unclosed subgrid viscous-work term $\sigma_{ij}^{\mathrm{sgs}}$ is assumed to be small and is neglected in the present study.

B. Thermodynamic and transport properties

Owing to the continuous variations of fluid properties throughout the jet and surroundings under supercritical conditions, conventional treatment of fluid jets at low pressures in which the liquid and gas phases are solved separately and then matched at the interfaces often leads to erroneous results. The problem becomes even more exacerbated when the fluid approaches its critical state, around which fluid properties exhibit anomalous sensitivities with respect to local temperature and pressure variations. Thus, a prerequisite of any realistic treatment of supercritical fluid behavior lies in the establishment of a unified property evaluation scheme valid over the entire thermodynamic regime.[3,14]

The formulation established here can accommodate any equation of state. In the present work, a modified Soave–Redlick–Kwong (SRK) equation of state is adopted because of its wide range of validity and ease of implementation.[19] It takes the following form:

$$p = \frac{\rho R_u T}{W - b\rho} - \frac{a\alpha}{W}\frac{\rho^2}{(W + b\rho)}, \tag{11}$$

where R_u is the universal gas constant. The parameters a and b account for the effects of attractive and repulsive forces between molecules, respectively. The third parameter α includes the critical compressibility factor and acentric (size-shape) interactions between molecules.

Thermodynamic properties, such as enthalpy, internal energy, and constant-pressure specific heat, can be expressed as the sums of ideal-gas properties at the same temperature and departure functions taking into account the dense-fluid correction.[3] Thus,

$$e(T,\rho) = e_0(T) + \int_{\rho_0}^{\rho}\left[\frac{p}{\rho^2} - \frac{T}{\rho^2}\left(\frac{\partial p}{\partial T}\right)_\rho\right]_T d\rho, \tag{12}$$

$$h(T,p) = h_0(T) + \int_{p_0}^{p}\left[\frac{1}{\rho} + \frac{T}{\rho^2}\left(\frac{\partial \rho}{\partial T}\right)_p\right]_T dp, \tag{13}$$

$$C_P(T,\rho) = C_{V0}(T) - \int_{\rho_0}^{\rho}\left[\frac{T}{\rho^2}\left(\frac{\partial^2 p}{\partial T^2}\right)_\rho\right]_T d\rho + \frac{T}{\rho^2}\left(\frac{\partial p}{\partial T}\right)_\rho^2 \Bigg/ \left(\frac{\partial p}{\partial \rho}\right)_T. \tag{14}$$

The subscript 0 refers to the ideal state at low pressure. The

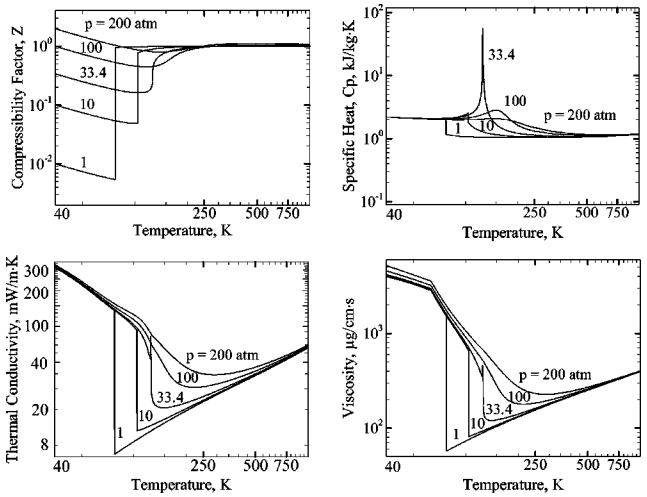

FIG. 2. Thermophysical properties of nitrogen as functions of pressure and temperature.

departure functions on the right-hand sides of Eqs. (12)–(14) can be determined from the equation of state.

Transport properties including viscosity and thermal conductivity are estimated by means of the corresponding state principles along with the use of the 32-term Benedict–Webb–Rubin equation of state.[20,21] Figure 2 shows the effects of temperature on the compressibility factor, specific heat, viscosity, and thermal conductivity of nitrogen in the temperature range of 40–1000 K at five different pressures of 1, 10, 33.4, 100, 200 atm. These figures illustrate key trends over the range of pressure and temperature of interest. At 750 K and above, nitrogen exhibits ideal gas behavior and the pressure effect is negligible. As the temperature decreases below 750 K however, significant nonidealities are introduced with strong pressure dependence. The implementation and validation of the property evaluation schemes were discussed in Ref. 3. It should be noted that the present scheme does not consider the critical enhancement in the close vicinity of the critical point, a region known as the critical region proper where a scaled equation of state must be used.[22] Thus, the thermophysical properties shown in Fig. 2 do not diverge at the critical point as predicted by classical theories. Since the simulation conditions chosen herein deviate considerably from the critical point, the neglect of critical divergence exerts no influence on the solution accuracy.

III. NUMERICAL METHOD

The present work bears two severe numerical challenges. First, thermodynamic nonidealities and transport anomalies take place as the fluid transits through the transcritical regime. Thus, treating these phenomena in a manner consistent with the intrinsic characteristics of a numerical algorithm presents a major obstacle. Second, the rapid variation of fluid state and wide disparities in the characteristic time and length scales pose the well-known stiffness problem. A unified treatment of general fluid thermodynamics is developed to circumvent those difficulties. The method is based on the concepts of partial-mass and partial-density properties,[14] and valid for the entire pressure and temperature regimes of concern. The resultant routine is incorporated into a preconditioning scheme along with a dual time-step integration algorithm to handle compressible fluid flows at all speeds.[23,24] Since all of the numerical relations, including the Jacobian matrices and eigenvalues, are derived directly from fundamental thermodynamics theories, the algorithm is self-consistent and robust. A detailed description of the overall approach was given by Meng and Yang.[14]

The theoretical formulation outlined above is solved by means of a density-based, finite volume methodology. The spatial discretization employs a fourth-order, central-difference scheme in generalized coordinates. A fourth-order scalar dissipation with a total-variation-diminishing switch developed by Swanson and Turkel[25] is implemented to ensure computational stability and to prevent numerical oscillations in regions with steep gradients. Temporal discretization is obtained using a second-order backward difference, and the inner-loop pseudotime term is integrated with a three-step third-order Runge–Kutta scheme. A multiblock domain decomposition technique, along with static load balance, is employed to facilitate the implementation of parallel computation with message passing interfaces at the domain boundaries.

IV. COMPUTATIONAL DOMAIN AND GRID SYSTEM

The physical model of concern is shown schematically in Fig. 1, simulating the experiments described in Refs. 10 and 12. Cryogenic nitrogen fluid is injected into supercritical gaseous nitrogen through a circular duct with an inner diameter of 0.254 mm. Because of the enormous computational effort required for calculating the flowfield in the entire three-dimensional regime, only a cylindrical sector with periodic boundary conditions specified in the azimuthal direction is treated herein. The analysis, in spite of the lack of vortex-stretching mechanism, has been shown to be able to capture the salient features of supercritical fluid jet evolution.[26]

The computational domain downstream of the injector measures a length of $40D_{\mathrm{inj}}$ and a radius of $6D_{\mathrm{inj}}$. The dimensions are sufficient to minimize the effect of the far-field boundary conditions on the near-injector flow evolution. The entire grid system consists 225×90 points along the axial and radial directions, respectively. The grids are clustered in the shear layer and near the injector to resolve rapid property variations in those regions. The mean grid size in the near field $(0\leqslant x/D_{\mathrm{inj}}\leqslant 20)$ falls in the inertial subrange of the turbulent kinetic energy spectrum, estimated using the Kolmogorov–Obukhow theory. The smallest grid width is 2 μm. The computational domain is divided into 45 blocks, with each calculated on a single processor of a distributed-memory parallel computer. The physical time step is 1×10^{-3} ms and the maximum Courant–Friedrich–Lewey number for the inner-loop pseudotime integration is 0.7. For each case, simulation was conducted for 12 flow-through times (i.e., 15 ms) to obtain statistically meaningful data.

A grid independence study was performed as part of the validation procedure, in which the same numerical code, configuration, and flow condition, i.e., case 1 in Table I) were

TABLE I. Simulation conditions.

	Case 1	Case 2	Case 3
P_∞ (MPa)	4.3	6.9	9.3
T_∞ (K)	300	300	300
ρ_∞ (kg/m^3)	46	77	103
T_{inj} (K)	120	120	120
ρ_{inj} (kg/m^3)	563	603	626
u_{inj} (m/s)	15	15	15
$\rho_{\text{inj}}/\rho_\infty$	12.24	7.83	6.07
Re	48 500	44 700	42 300

considered with two different grid resolutions: a fine (270×120) and a coarse (225×90) mesh. Figure 3 shows the radial distributions of the mean axial velocity, turbulent kinetic energy (TKE), compressibility factor Z, and viscosity (normalized by the value of the ambient gas) at different axial locations. Results from the two different grid systems agree well with each other, except for the small deviation of TKE.

V. BOUNDARY CONDITION

At the injector exit, a fully developed turbulent pipe flow is assumed. The mean velocity follows the one-seventh-power law and the temperature is specified with a top-hat profile. The pressure is determined using a one-dimensional approximation to the momentum equation in the axial direction. Turbulence is provided by superimposing broadband white noise onto the mean velocity profile. The disturbances are generated by a Gaussian random-number generator with an intensity of 12% of the mean quantity. At the downstream boundary, extrapolation of primitive variables from the interior may cause undesired reflection of waves propagating into the computational domain. Thus, the nonreflecting boundary conditions proposed by Poinsot and Lele[27] are applied, along with the specification of a reference pressure. Because the jet flow is directly exhausted to an ambient condition, the surrounding fluid may be entrained into the computational domain. At the radial boundary, the pressure, temperature, and axial velocity are specified. The conservation law of mass is employed to determine the radial velocity. Finally, the nonslip adiabatic conditions are enforced along the solid walls.

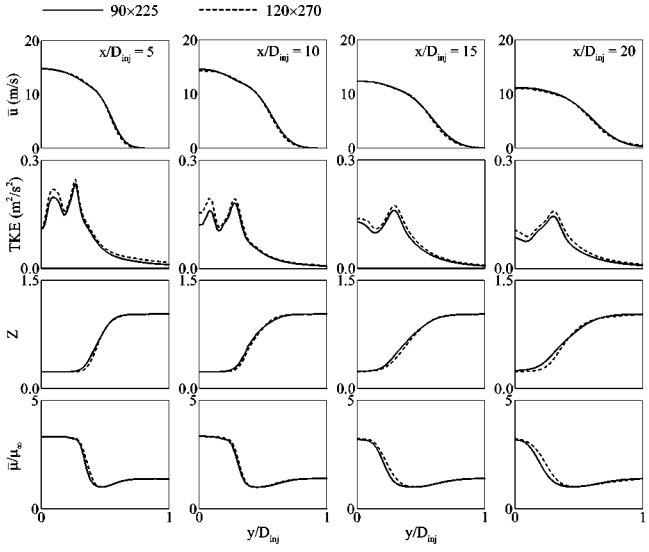

FIG. 3. Effect of grid resolution on radial distributions of mean axial velocity, turbulent kinetic energy, compressibility factor, and viscosity at different axial locations (p_∞=4.3 MPa, T_∞=300 K, u_{inj}=15 m/s, T_{inj}=120 K, D_{inj}=254 μm), — 90×225 mesh, - - - 120×270 mesh.

VI. RESULTS AND DISCUSSIONS

The theoretical model and numerical scheme established in the preceding sections were implemented to study the injection and mixing of cryogenic fluid under supercritical conditions. As a specific example, liquid nitrogen at a temperature of 120 K is injected through a circular tube with a diameter of 254 μm into a supercritical nitrogen environment. A turbulent pipe flow with a bulk velocity of 15 m/s is assumed at the injector exit. The ambient temperature remains at 300 K, but the pressure varies from 42 to 93 atm, comparable to the chamber pressures of many operational rocket engines. For reference, the critical temperature and pressure of nitrogen are 126 K and 34 atm, respectively. Three different flow conditions summarized in Table I are considered, simulating the experiments conducted by Chehroudi and Talley,[10] where the subscripts ∞ and inj denote the injection and ambient conditions, respectively. The Reynolds number is defined as $\text{Re}=\rho_{\text{inj}}u_{\text{inj}}D_{\text{inj}}/\mu_{\text{inj}}$

Figure 4 shows the variations of nitrogen density and constant-pressure specific heat as functions of temperature at four different pressures. Two observations are noted here. First, the density decreases sharply near the critical point as the temperature increases. The effect of density stratification between the jet and the ambient fluid becomes much more substantial for p_∞=4.3 MPa compared with the other two cases. Second, the temperature sensitivity of the specific heat depends strongly on pressure. It increases rapidly as the fluid state approaches the critical point, and theoretically becomes infinite exactly at the critical point. This implies that much more thermal energy is needed to heat up the cold fluid jet in case 1 (i.e., p_∞=4.3 MPa) than the other two cases when the fluid temperature transits across the near-critical regime. The anomalous variations of fluid volumetric and thermal properties near the critical point and their dependence on pressure have profound influences on fluid jet development at high pressures.

A. Instantaneous flowfield

For a constant-density jet, the shear layer between the jet and the ambient fluid is susceptible to the Kelvin–Helmholz instability and experiences vortex rolling, paring, and breakup. A cryogenic supercritical jet undergoes qualitatively the same process, but with additional mechanisms arising from volume dilation and baroclinic torque.

Figure 5 shows snapshots of the density, density-gradient, temperature, and vorticity-magnitude fields at three different ambient pressures. The small vortical structures in the core region result from the imposed turbulent motions at

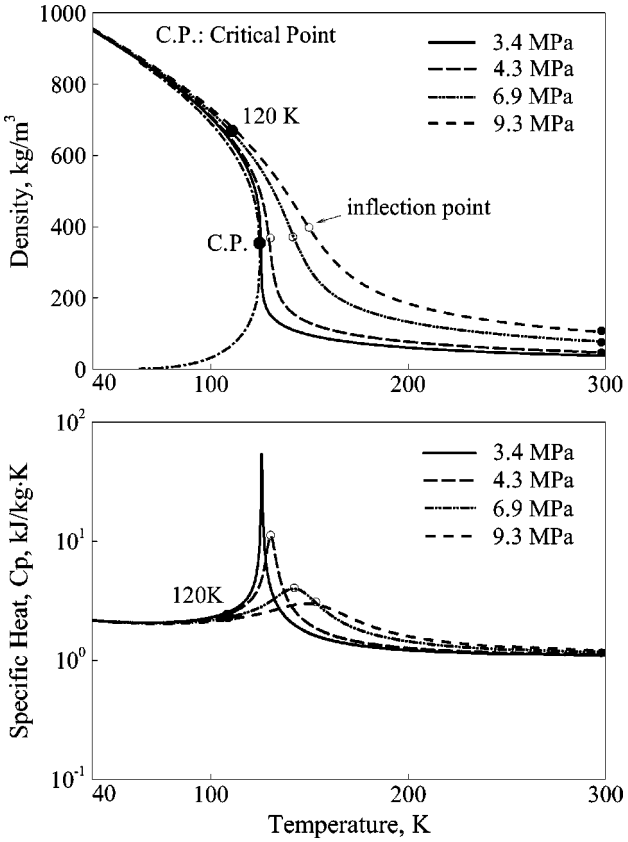

FIG. 4. Density and constant-pressure specific heat of nitrogen as the functions of temperature and pressure.

the injector exit. For case 1, in which the ambient pressure of 4.3 MPa is closer to the critical value, the jet surface is straight near the injector with only tiny instability waves in the downstream region. As the ambient pressure increases, the velocity fluctuation in the radial direction becomes more vigorous. Large-scale instability waves develop in the near-injector region, which then grow up and roll into a succession of ring vortices as the injected fluid moves downstream. The resultant vortical flow motions facilitate the entrainment of the ambient gaseous nitrogen into the cold jet fluid. The initial density-stratification layer is only slightly stretched in case 1, but severely twisted in higher-pressure cases. As a general trend, the higher the ambient pressure, the stronger vortical motions and radial velocity fluctuations near the jet surface.

It has been established[28] that the evolution and interaction of large coherent structures strongly influence the mixing and entrainment of a shear layer. Figure 6 shows the temporal evolution of the jet surface structures of case 3 ($p_\infty = 9.3$ MPa). Both the temperature and density fields clearly demonstrate the entrainment of lighter and warmer ambient gaseous nitrogen into the jet flow through vortical motions, along with a series of thread-like entities emerging from the jet surface. The same phenomena were observed in the experiments by Chehroudi and co-works under the same flow condition.[10]

B. Effect of density stratification

To explore the formation and influence of the density-stratification layer near the jet boundary, conditional-averaged temperatures over the regions where the density-gradient magnitudes exceed prespecified cutoff values are determined. The result is listed in Table II, where $|\nabla\rho|_{\max}$ is the maximum density gradient in the entire field, around 1.15×10^7 kg/m^4 for case 3. The conditional fluid temperature decreases with increasing cutoff density gradient, and approaches the inflection point on the isobaric ρ-T curve shown in Fig. 4. Table III summarizes the inflection temperatures for the three different pressures considered herein. It is noteworthy that fluid properties usually undergo rapid variations across the temperature inflection point for an isobaric process, and the specific heat reaches its maximum at this point. For example, the density of nitrogen decreases more than three times in case 1 as the temperature increases from 125 to 135 K Thus, the formation of the steep density-gradient region is closely related to property variations, which to a large extent are dictated by real-fluid thermodynamics. Turbulent diffusion and mixing tend to introduce warm ambient gases into the cold jet, and subsequently smooth the density-stratification effect. The drastic volume dilation during the mixing process when the temperature transits across the inflection point, however, prevents the entrainment of the surrounding fluid, and thereby facilitates the formation of steep density-gradient regimes.

The effect of density stratification on the evolution of a planar mixing layer was studied by Atsavapranee and Gharib.[29] Because the higher density stratification increasingly inhibits instability-wave growth and vortex paring, the flow topography is considerably simplified, as evidenced in Fig. 5. In addition, the total yield of mixed fluid is reduced with high density stratification due to the combined effect of weakened, fluid entrainment into the Kelvin–Helmholtz vortices, decreased frequency of vortex paring, and arrest of turbulence during flow restratification.

Figure 7 shows the power spectral densities (PSD) of the axial and radial velocity fluctuations at various radial locations of $r/D_{\text{inj}} = 0.6$, 0.7, and 0.8 in the mixing layer for $p_\infty = 9.3$ MPa. The axial position of $x/D_{\text{inj}} = 16$ is near the end of the potential core, where a sharp density gradient exists at $r = 0.1\,D_{\text{inj}}$ (see Fig. 5). In the low-frequency regime, in which large-scale structures prevail, the axial velocity fluctuation increases as the density stratification layer is approached. The trend for the radial velocity fluctuation, however, is opposite. The velocity fluctuations in the high-frequency range remain basically insensitive to the radial position. Density stratification exerts a strong influence on large-scale flow motions. It acts like a solid wall in the flow that amplifies the axial turbulent fluctuation but damps the radial one. The same PSD results are also observed for cases 1 and 2, which are not presented here.

A similar phenomenon was reported by Hannoun, Ferrando, and List[30] in their experiments on grid-induced shear-free turbulence near a sharp density interface. As a consequence of the strong anisotropy of the turbulence near the density interface, large eddies of integral length scales be-

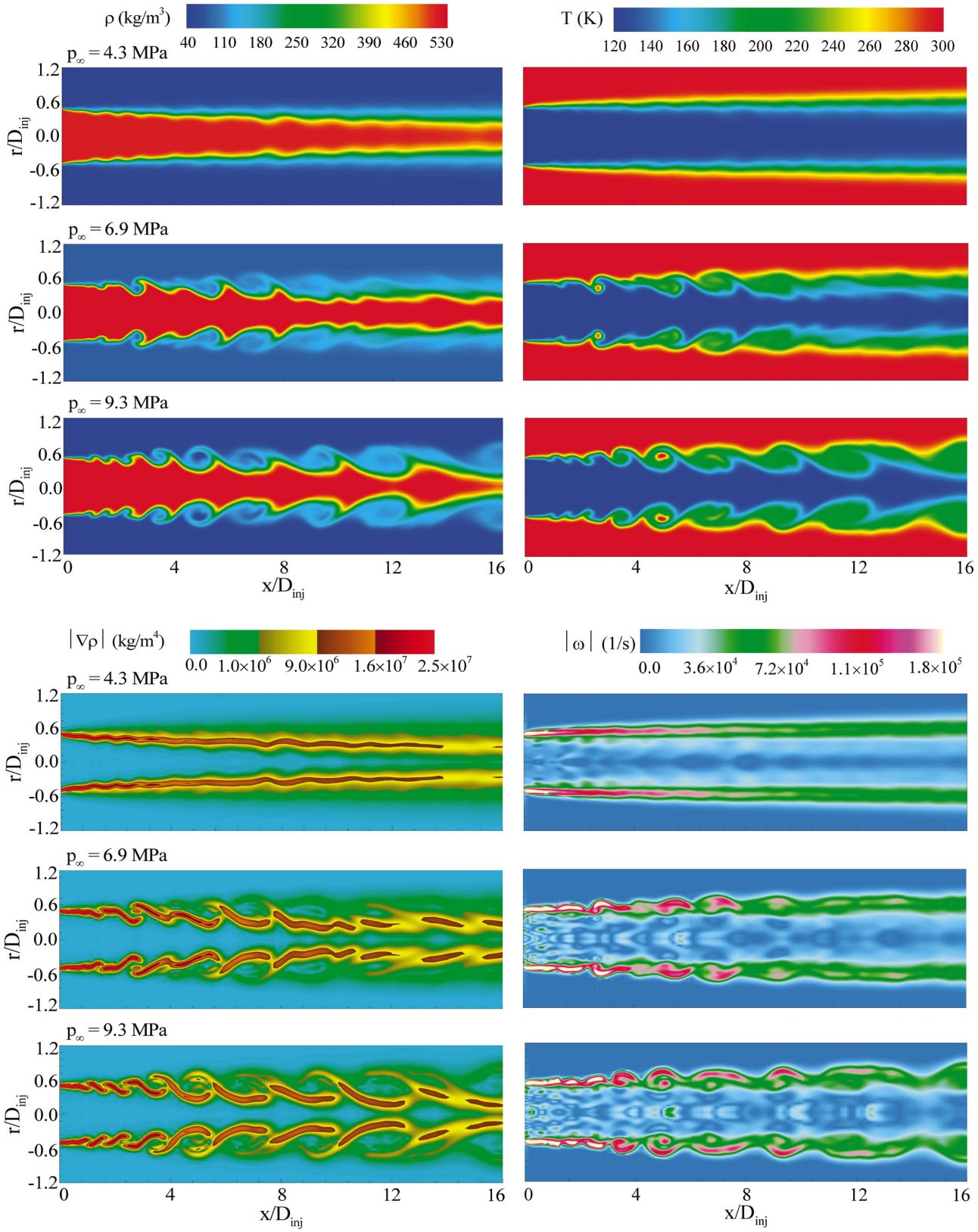

FIG. 5. (Color). Effect of pressure on density, density-gradient, temperature, and vorticity fields (T_∞=300 K, u_{inj}=15 m/s, T_{inj}=120 K, D_{inj}=254 μm, t=1.55 ms).

come flattened, and the vertical component of the turbulent kinetic energy is transferred to its horizontal quantity. Such an energy redistribution among its spatial components considerably modifies the amount of energy available for fluid mixing at the density interface. Thus, the existence of strong density stratification suppresses radial velocity fluctuations in the flowfield and inhibits the development of instability waves. In the present study, the initial density ratio and the

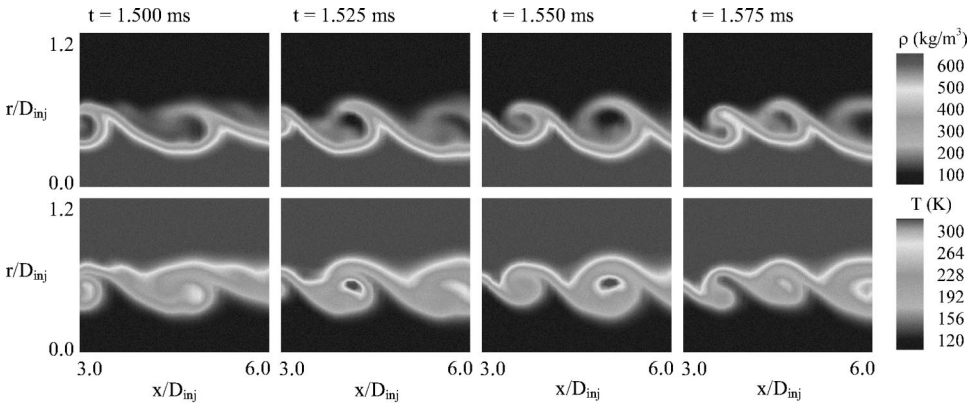

FIG. 6. Time evolution of jet surface structures (p_∞=9.3 MPa, T_∞=300 K, u_{inj}=15 m/s, T_{inj}=120 K, D_{inj}=254 μm).

strength of density stratification decrease as the ambient pressure increases, so do their damping effects on the shear layers. The jet surface is nearly straight in case 1, with only tiny instability waves developing in the downstream region. The shear layers, however, are highly twisted in both cases 2 and 3, as shown in Fig. 5.

The frequency spectra of velocity fluctuations shown in Fig. 7 do not indicate the standard 5/3 law for the turbulent kinetic energy spectrum based on the Kolmogorov theory, which characterizes the inertial subrange. Apte and Yang[31] mentioned in their two-dimensional simulations of unsteady flow evolution in a porous-walled chamber that the exponent of the wave number, in the inertial subrange of the turbulent energy spectrum varies between f^{-3} and f^{-4}, with f being the frequency. Gilbert[32] proposed that the kinetic energy spectrum can be obtained from spiral vortex distributions within coherent vortices and should follow the $f^{-11/3}$ law. In this work, the frequency dependence in the inertial subrange lies between $f^{-5/3}$ and f^{-3}.

The present two-dimensional large-eddy simulation inherently neglects the vortex stretching mechanism, which is responsible for the transfer of energy from large to small scales through energy cascade and the continuous generation of small-scale vortical structures. Since these structures redistribute and dissipate energy at the smallest scales, the lack of vortex stretching leads to lower energy dissipation and turbulence-production rates during the flow evolution. This issue will be addressed in subsequent three-dimensional calculations.

C. Shear-layer instability

To study the vortical dynamics and flow instability in the mixing layer, the power spectral densities of the radial velocity oscillations at two different axial locations are presented in Fig. 8. The radial position is fixed at r/D_{inj}=0.5. A dominant frequency around 35 kHz, corresponding to the most amplified frequency of the shear layer instability, is observed at an upstream location of x/D_{inj}=8 for both cases 2 and 3. This frequency is weakly dependent on the ambient pressure (or the density ratio). When the fluid is convected downstream to x/D_{inj}=18, the dominant frequency decreases to 15.9 kHz for case 2 and 18.6 kHz for case 3, nearly one-half of the value of the most amplified shear instability mode. The vortex pairing process is clearly demonstrated. The situation, with case 1, however, is considerably different. Owing to the low compressibility factor (i.e., 0.21) of the injected fluid and the large density ratio of 12.24, the jet exhibits a liquid-like fluid behavior distinct from the other high-pressure cases. The dominant frequencies become 20 and 10 kHz at x/D_{inj}=8 and 18, respectively.

The flow instabilities and vortex shedding in constant-density shear layers were reviewed by Schadow and Gutmark.[33] Based on their work, the initial vortex shedding frequency f_1 can be scaled with the shear-layer momentum thickness θ_0 and characteristic velocity $\bar{U}$, normally taken as the average bulk velocity of the two streams. The result yields a nondimensional frequency or Strouhal number, $St_i = f_i\theta_0/\bar{U}$, which ranges from 0.044 to 0.048 for a planar turbulent shear layer. As the vortices move downstream, they merge together to oscillate at the subharmonics of the initial vortex shedding frequency, $f_1/N(N=2, 3, 4)$. Although the above analysis was formulated for planar flows, it can be applied with good accuracy to mixing layers in axisymmetric configurations if the thickness of the shear layer is much smaller than the radius of the injector. In the present work, $\bar{U}\approx 8$ m/s and the initial momentum thickness θ_0 estimated for a fully developed turbulent pipe flow is 0.011 mm. If the Strouhal number is chosen to be St_i=0.048, then the most amplified frequency becomes f_1=34.9 kHz and the corresponding second harmonic frequency is 17.5 kHz. Those val-

TABLE II. Conditional averaged temperatures (K) in regions with $|\nabla\rho|$>cutoff value.

Cutoff	Case 1	Case 2	Case 3
$0.1\|\nabla\rho\|_{max}$	131.7	151.0	158.0
$0.2\|\nabla\rho\|_{max}$	131.1	148.0	154.0
$0.3\|\nabla\rho\|_{max}$	130.6	145.5	151.3

TABLE III. Temperature at inflection points on isobaric ρ-T curves at different pressures.

	Case 1	Case 2	Case 3
P_∞ (MPa)	4.3	6.9	9.3
T (K)	130.3	142.1	148.6

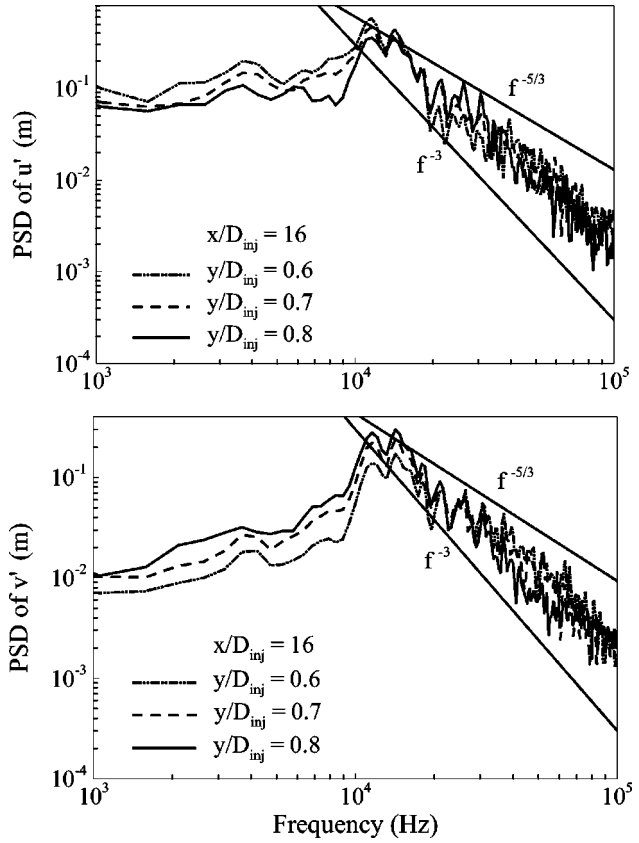

FIG. 7. Power spectral densities of velocity fluctuations at different radial locations with $x/D_{\mathrm{inj}}=16$ ($p_\infty=9.3$ MPa, $T_\infty=300$ K, $u_{\mathrm{inj}}=15$ m/s, $T_{\mathrm{inj}}=120$ K, $D_{\mathrm{inj}}=254$ μm).

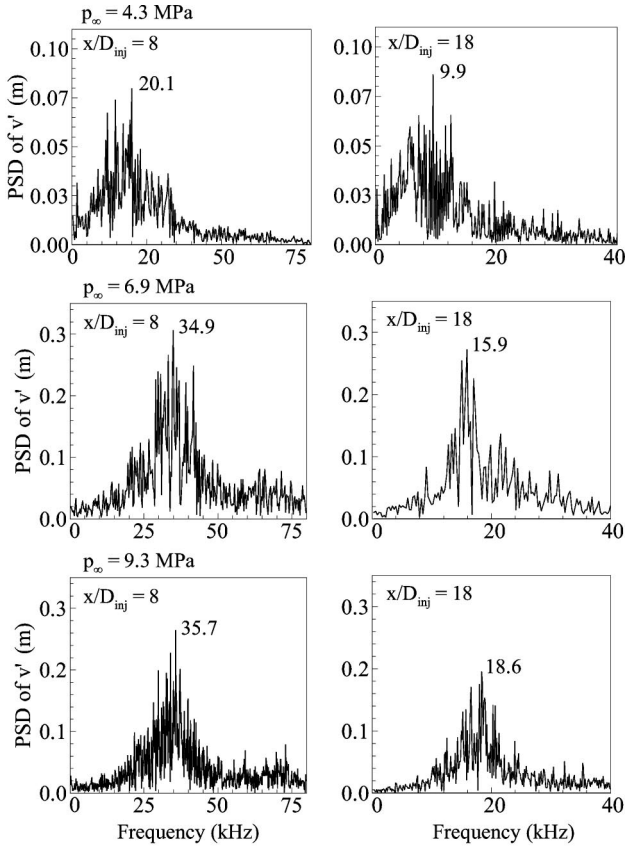

FIG. 8. Effect of pressure on power spectral densities of radial velocity fluctuations at two different axial locations with $r/D_{\mathrm{inj}}=0.5$.

ues agree well with the calculated vortex-shedding frequencies based on the radial velocity oscillations in cases 2 and 3.

To provide more insight into observed flow phenomena, a linear stability analysis is carried out of the effects of ambient pressure on the fluid jet evolution. The work extends the approaches described in Refs. 34 and 35 to include real-fluid thermodynamics. The SRK equation of state is implemented in the formulation. Each dependent variable is decomposed into a base and a perturbation quantity. The former is adopted directly from the present simulation. The latter takes the following general form for a planar jet:

$$\hat{\phi}(x,y,t)=\phi(y)\ \exp\{i(kx-\omega t)\}, \tag{15}$$

where k and ω are the wave number and frequency, respectively. For a spatial instability problem, k is a complex variable and its negative imaginary part represents the spatial growth rate. After substitution of the decomposed variables into the conservation laws and linearization of the result, a dispersion equation characterizing the relationship between the wave number and frequency can be derived in terms of pressure fluctuation as follows:

$$\frac{d^2\hat{p}}{dy^2}-\left(\frac{1}{\overline{\rho}}\frac{d\overline{\rho}}{dy}+\frac{2}{\overline{u}-\omega/k}\frac{d\overline{u}}{dy}\right)\frac{d\hat{p}}{dy}-k^2\hat{p}=0. \tag{16}$$

The problem now is solving Eq. (16) for the eigenvalues k and ω subject to appropriate boundary conditions. A complete discussion of the stability analysis is given in Ref. 36.

Figure 9 shows the spatial growth rates of the instability waves as a function of the normalized frequency (i.e., the Strouhal number) for the three different pressures considered in the present study. The growth rate of the shear wave decreases with increasing pressure. The strong density stratification in the lower-pressure case suppresses the growth of the wave and stabilizes the mixing layer. The theoretically predicted frequencies of the most unstable oscillations are 23.2, 28.8, and 29.6 kHz for cases 1, 2, and 3, respectively. These values are slightly underestimated for cases 2 and 3, but overestimated for case 1. The maximum deviation from the numerical simulation is 15%. The frequency of the most unstable mode exhibits a weak pressure dependence at high pressures. It, however, decreases significantly in the near-critical regime due to the enhanced effect of density stratification and increased mixing-layer momentum thickness.

D. Vortical dynamics

As a consequence of the large velocity difference between the jet and ambient flow, a strong shear layer is generated near the injector, which is then tilted and develops to large structures due to vortex interactions. The vortical dynamics can be best quantified using the transport equation given below,

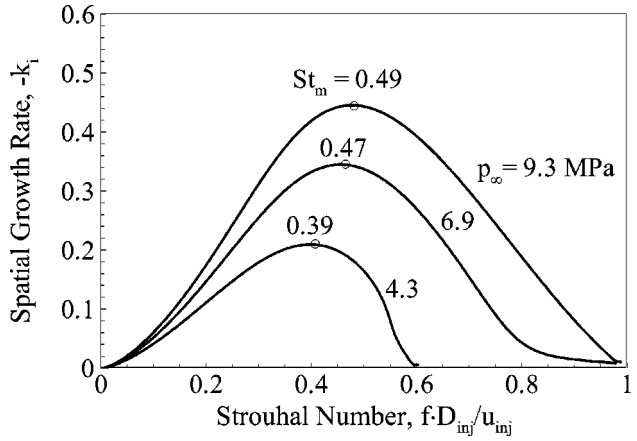

FIG. 9. Spatial growth rate as function of Strouhal number at different pressures.

$$\frac{D\boldsymbol{\omega}}{Dt} = (\boldsymbol{\omega}\cdot\nabla)\boldsymbol{u} - (\nabla\cdot\boldsymbol{u})\boldsymbol{\omega} - \boldsymbol{\nabla}\left(\frac{1}{\rho}\right) \times\boldsymbol{\nabla} p + \boldsymbol{\nabla}\times\left(\frac{1}{\rho}\nabla\cdot\boldsymbol{\tau}\right), \tag{17}$$

where D/Dt stands for the substantial derivative. The first term on the right-hand side represents vortex stretching, which vanishes in the present two-dimensional simulation. The second term describes the volume-dilatation effect, and the third term denotes the baroclinic torque produced by the misalignment between the pressure and density gradients. The last term arises from viscous dissipation. For cryogenic fluid injection under supercritical conditions, large volume expansion occurs when the jet is heated by the ambient gas. Thus, both baroclinic torque and volume dilatation may play an important role in determining vorticity transport.

Figure 10 shows an instantaneous azimuthal vorticity budget in the radial direction at the axial position of $x/D_{\mathrm{inj}}=5$ for all the three cases. At this position, the large coherent structures are well developed in cases 2 and 3. The results are normalized by the bulk velocity (u_{inj}) and momentum thickness (θ_0) at the injector exit. The baroclinic torque and viscous dissipation locally rival in magnitude, and have opposite contributions in Eq. (17). These two terms attain their maxima in regions with large density gradients in which vigorous mixing between the jet and ambient flows occurs (see Fig. 5). In case 1, much of the vorticity production takes place on the light fluid side. A similar phenomenon was noted by Okong'o and Bellan in their study of a supercritical binary mixing layer.[15] As the ambient pressure increases (or the density ratio decreases), the location with intensive vorticity production slightly shifts toward the dense fluid, but still resides on the ambient gas side, since the radial position of the mixing region also changes. The magnitudes of all the three vorticity production terms increase with increasing ambient pressure due to strengthened vortical motions.

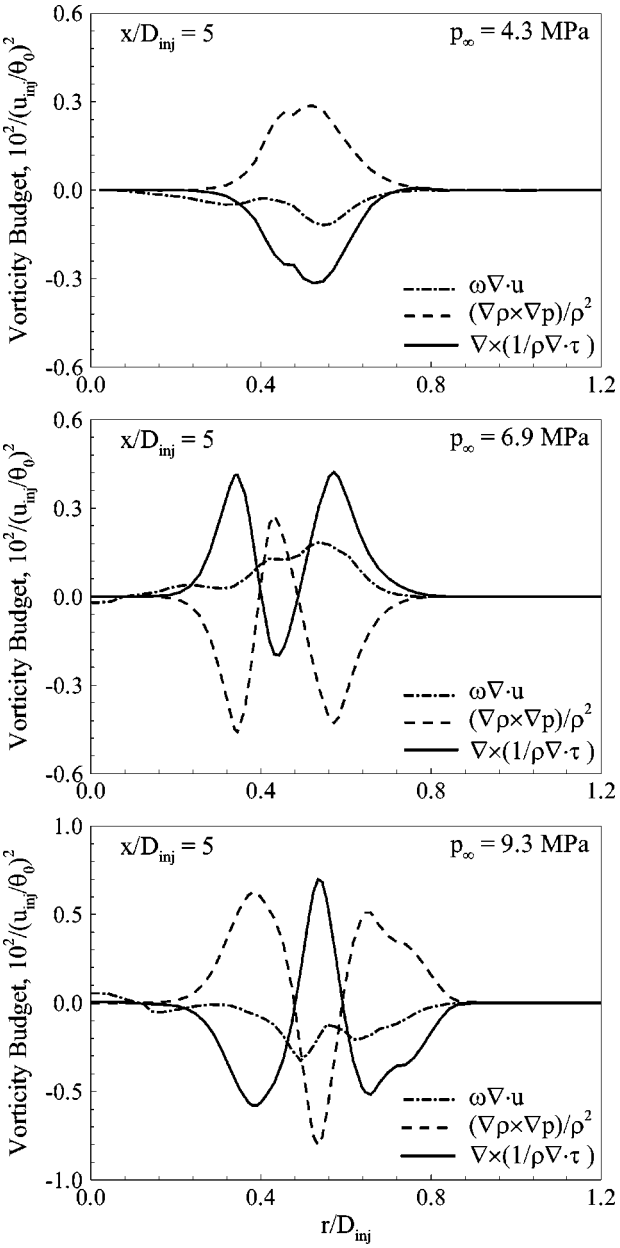

FIG. 10. Vorticity budgets at different ambient pressures ($T_\infty=300$ K, $u_{\mathrm{inj}}=15$ m/s, $T_{\mathrm{inj}}=120$ K, $D_{\mathrm{inj}}=254$ μm, $t=1.55$ ms).

E. Mean flow properties

The mean flow properties are obtained by taking long-time average of the instantaneous quantities over 10 ms (about eight flow-through times) after the calculated flowfield has reached its stationary state. Figure 11 shows the radial distributions of the normalized mean density, $\rho^+=(\overline{\rho}-\overline{\rho_\infty})/(\overline{\rho_c}-\overline{\rho_\infty})$, at six different axial locations. The subscript c refers to the quantity at the centerline. The radial coordinate is normalized by the full width of the radial profile measured where the flow property of concern (i.e., density in the present figure) is one half of its maximum value (FWHM), $r_{1/2}$. Similar to incompressible fluid jets, there exist three distinct regions in a cryogenic fluid jet under supercritical conditions: a potential core in the upstream where a flat-hat distribution around the centerline occurs, a transition region, and a fully developed self-similar region. The density profiles at $x/D_{\mathrm{inj}}>25$ merge to a single distribution for cases 2 and 3, manifesting the existence of self-similarity in the downstream region. Such a self-similar profile, however, is

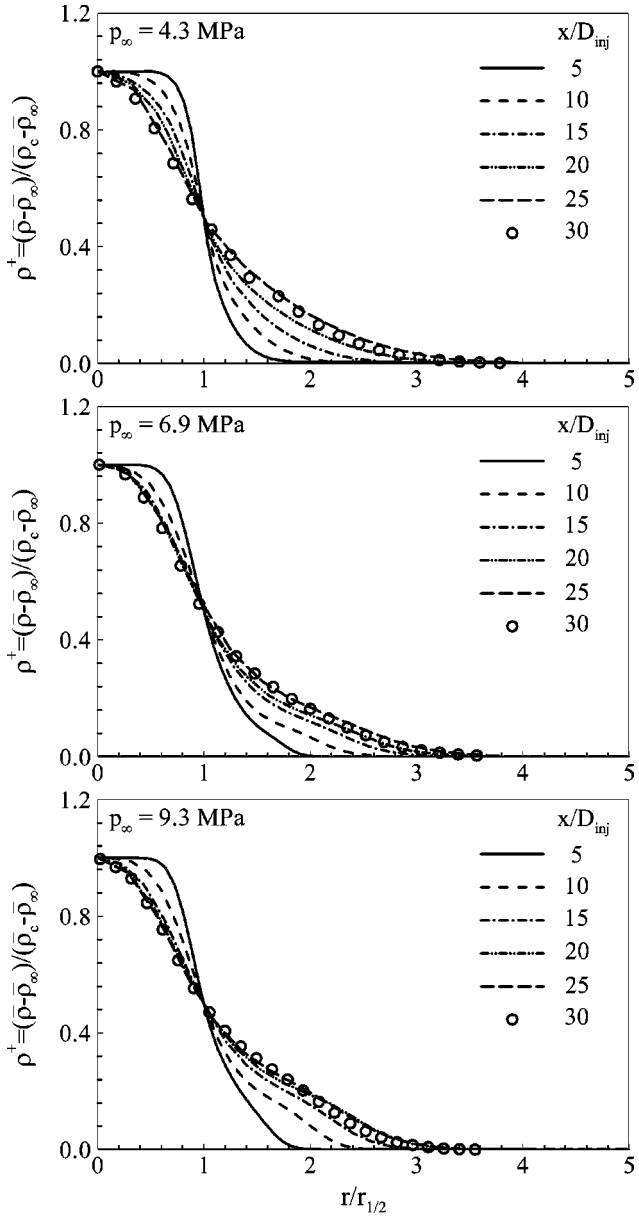

FIG. 11. Effect of pressure on normalized density distribution in radial direction.

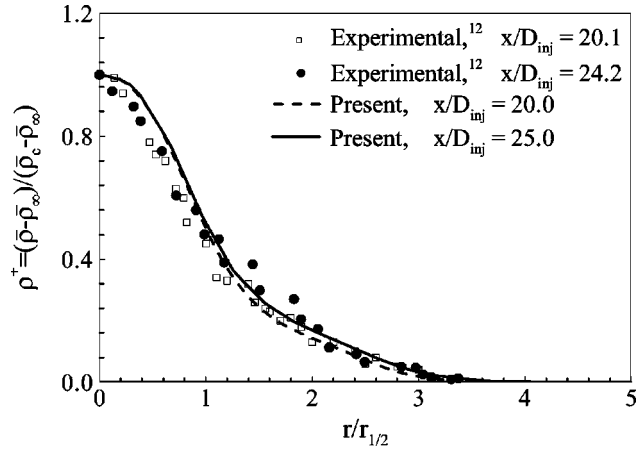

FIG. 12. Comparison of calculated and measured density profiles at different axial locations.

not observed until $x/D_{\text{inj}} > 30$ for case 1. The high-pressure condition facilitates the development of the self-similar behavior through its effect on reducing the density ratio of the injected fluid to the ambient flow. Figure 12 shows the comparison with the density field measured by Chehroudi and Talley[12] using the Raman scatting technique under the same condition of case 2 ($p_\infty = 6.9$ MPa). The calculated and measured radial distributions follow exactly the same trend at the two positions. The maximum deviation is 5%.

Figure 13 shows the normalized axial velocity profiles in the radial direction. Self-similarity is achieved at the same location as that for the density distribution. It occurs at a relatively upstream position as the ambient pressure increases. Compared with the density field, the velocity profile exhibits a narrower distribution, with the jet boundary (defined as the radial position at which $u = 0.01u_c$) situated at $r/r_{1/2} \approx 2.5$, a value consistent with the data reported in Ref. 9. In addition, no flat-hat profile exists even in the upstream region due to the use of the one-seventh power distribution for a fully developed turbulent pipe flow at the injector exit.

Figure 14 presents the axial distributions of the normalized temperature, density, and compressibility factor along the centerline for three different pressures. Evidently, the temperature decreases relatively slowly with decreasing pressure in the axial direction. It is well established that when a fluid reaches its thermodynamic critical state, the constant-pressure specific heat becomes infinite and the thermal diffusivity decreases to zero, a phenomenon known as the critical divergence. Because the ambient pressure for case 1 ($p_\infty = 4.3$ MPa) is closer to the critical value, the specific heat increases drastically when the temperature transits across the inflection point on the isobaric ρ-T curve (see Fig. 4). This effect, combined with the lower thermal conductivity, causes a slower increase in temperature along the centerline in case 1 as the injected fluid moves downstream. The compressibility factor, shown in Fig. 2, indicates a monotonic decrease with decreasing pressure in the low-temperature regime, and a rapid increase across the inflection point on the isobaric ρ-T curve. The compressibility factor, thus, increases much more rapidly at a lower pressure, which amounts to a faster decrease in density. Although the centerline temperature varies laggardly in all the three cases, the rapid variation of the compressibility factor causes the density to undergo a fast decrease downstream of the potential core, especially for the case of $p_\infty = 4.3$ MPa.

The rapid variations of thermophysical properties exert a significant influcence on the jet flow evolution. Figure 15 shows the radial distributions of the specific heat, thermal diffusivity, and kinematic viscosity at $x/D_{\text{inj}} = 10$, a location slightly upstream of the end of the potential core. A spike exists in the specific-heat profile at $r/r_{1/2} = 0.6$ in case 1, mainly due to the temperature transition across the inflection point. The same phenomenon is observed for cases 2 and 3, but with much lower amplitudes. The thermal diffusivity also exercises a large excursion of variation across the temperature inflection point. It increases considerably from the liquid core to the ambient flow by a factor of l4, 7, and 5 in cases 1, 2, and 3, respectively. A similar situation occurs with the

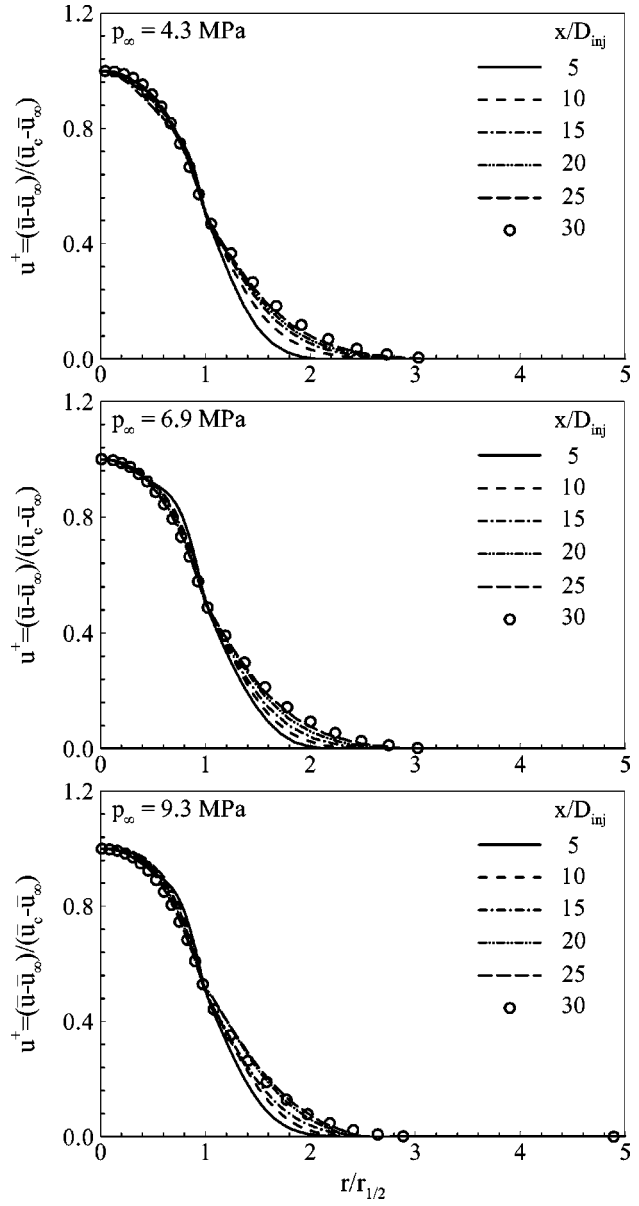

FIG. 13. Effect of pressure on normalized velocity distribution in radial direction.

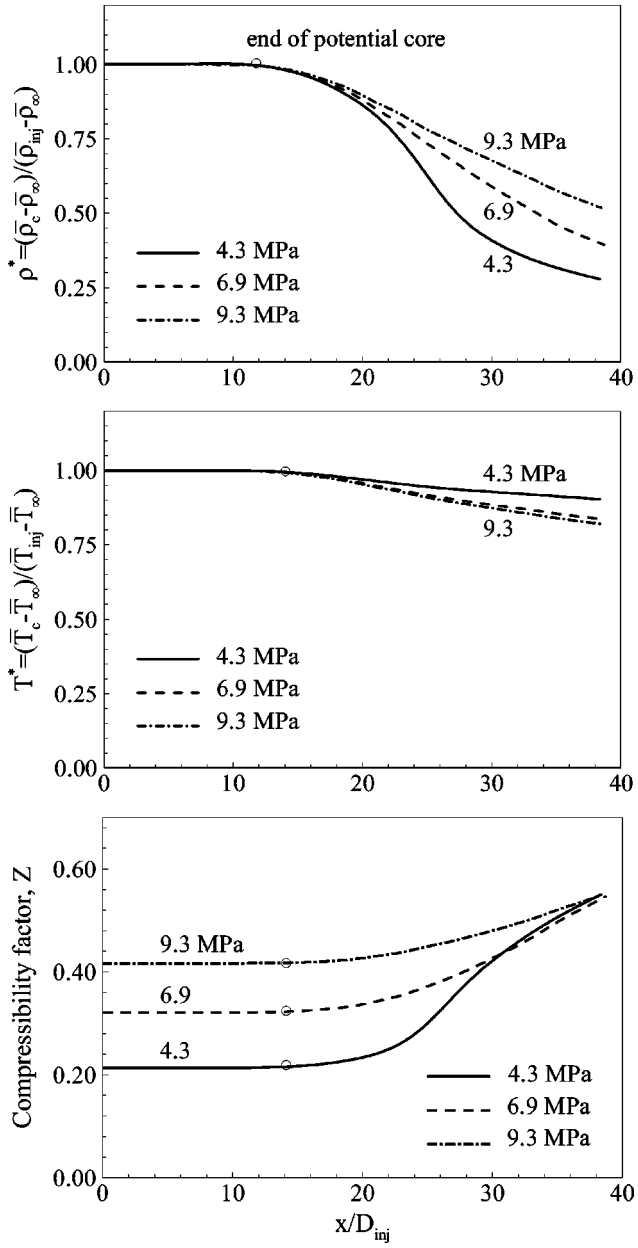

FIG. 14. Effect of pressure on normalized density, normalized temperature, and compressibility factor along jet centerline.

kinematic viscosity. The intensive change of viscosity in the shear layer gives rise to another vorticity production mechanism, as shown in Eq. (17). These observations, again, highlight the importance of thermophysical properties in dictating the behavior of a supercritical fluid jet.[37]

VII. CONCLUSIONS

A comprehensive numerical study has been conducted to investigate cryogenic fluid injection and mixing under supercritical conditions. The model accommodates full conservation laws and real-fluid thermodynamics and transport phenomena over the entire range of fluid states of concern. Turbulent closure is achieved using a large-eddy-simulation technique. The present analysis allows a detailed investigation into the temporal and spatial evolution of a cryogenic jet. The near-field behavior is well captured.

The major results obtained are summarized below.

(1) As a result of intensive property variations between the fluid jet and surroundings, a series of large density-gradient regions are formed around the jet surface. These regions act like a solid wall that amplifies the axial flow oscillations but damps the radial ones. The interfacial instability in the shear layer is effectively suppressed, especially for cases with large density ratios. As the ambient pressure increases, the strength of density stratification decreases, so does its damping effect. Thus, the jet expands rapidly with increasing pressure.

(2) Various mechanisms dictating vorticity transport are analyzed. The baroclinic torque arising from the density stratification between the injected and ambient flows and viscous dissipation play an important role in determining the flow evolution.

(3) The jet dynamics are largely dictated by the local

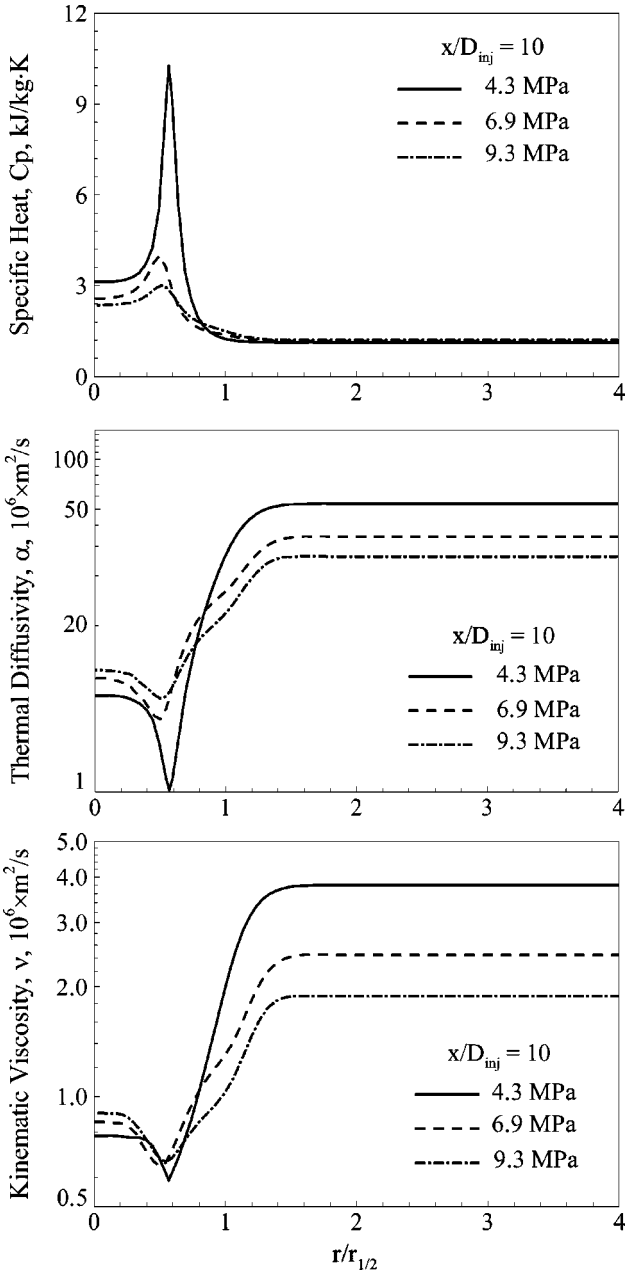

FIG. 15. Radial distributions of mean thermophysical properties at $x/D_{\mathrm{inj}} = 10$.

thermodynamic state of the fluid. When the temperature transits across the inflection point in an isobaric process, the rapid property variations may qualitatively change the jet behavior compared with its counterpart at low pressures. In addition, an increase in the ambient pressure may result in an earlier transition of the jet into the self-similar region.

(4) The spatial growth rate of the surface instability wave increases as the ambient pressure increases. The frequency of the most unstable mode exhibits a weak pressure dependence at high pressures. It, however, decreases significantly in the near-critical regime due to the enhanced effect of density stratification and increased mixing-layer momentum thickness. The result agrees well with the linear stability analysis.

ACKNOWLEDGMENTS

This work was sponsored by the Air Force Office of Scientific Research, Grant No. F49620-01-1-0114. The authors gratefully acknowledge the support from Dr. Mitat A. Birkan, contract monitor of the program.

[1] J. M. H. Levelt Senger, "Thermodynamics of solutions near the solvent's critical point," in *Supercritical Fluid Technology*, edited by T. J. Bruno and J. F. Ely (CRC Press, Boca Raton, FL, 1991), Chap. 1.
[2] J. C. Oefelein and V. Yang, "Modeling high-pressured mixing and combustion processes in liquid rocket engines," J. Propul. Power **114**, 843 (1998).
[3] V. Yang, "Modeling of supercritical vaporization, mixing, and combustion processes in liquid-fueled propulsion systems," Proc. Combust. Inst. **28**, 925 (2000).
[4] J. Bellan, "Supercritical (and subcritical) fluid behavior and modeling: drops, streams, shear and mixing layers, and sprays," Prog. Energy Combust. Sci. **26**, 329 (2000).
[5] J. A. Schetz, "Injection and mixing in turbulent flow," in *Progress in Astronautics and Aeronautics*, edited by M. Summerfield (American Institute of Aeronautics and Astronautics, Washington, DC, 1980), Vol. 68, p. 19.
[6] G. N. Abramovich, *The Theory of Turbulent Jets* (MIT Press, Cambridge, MA, 1963).
[7] J. A. Newman and T. A. Brzustowski, "Behavior of a liquid jet near the thermodynamic critical region," AIAA J. **19**, 1595 (1971).
[8] W. Mayer, A. Schik, M. Schäffler, and H. Tamura, "Injection and mixing processes in high pressure liquid oxygen/gas hydrogen rocket combustors," J. Propul. Power **16**, 823 (2000).
[9] R. Branam and W. Mayer, "Characterization of cryogenic injection at supercritical pressure," J. Propul. Power **19**, 342 (2003).
[10] B. Chehroudi, D. Talley, and E. Coy, "Visual characteristics and initial growth rates of round cryogenic jets at subcritical and supercritical pressures," Phys. Fluids **14**, 850 (2002).
[11] M. Oschwald and A. Schik, "Supercritical nitrogen free jet investigated by spontaneous Raman scattering," Exp. Fluids **27**, 497 (1999).
[12] B. Chehroudi, R. Cohn, D. Talley, and A. Badakhshan, "Cryogenic shear layers: Experiments and phenomenological modeling of the initial growth rate under subcritical and supercritical conditions," Int. J. Heat Fluid Flow **23**, 554 (2002).
[13] B. Chehroudi and D. Talley, "Interaction of acoustic waves with a cryogenic nitrogen jet at sub- and super-critical pressures," AIAA Paper No. 2002–0342, 40th AIAA Aerospace Sciences Meeting and Exhibit, Reno, NV, January 2002.
[14] H. Meng, and V. Yang, "A unified treatment of general fluid thermodynamics and its application to a preconditioning scheme," J. Comput. Phys. **189**, 277 (2003).
[15] N. A. Okong'o and J. Bellan, "Direct numerical simulation of a transitional supercritical binary mixing layer: Heptane and nitrogen," J. Fluid Mech. **464**, 1 (2002).
[16] R. S. Miller, K. G. Harstad, and J. Bellan, "Direct numerical simulations of supercritical fluid mixing layers applied to heptane–nitrogen," J. Fluid Mech. **436**, 1 (2001).
[17] N. A. Okong'o, K. G. Harstad, and J. Bellan, "Direct numerical simulation of O2/H2 temporal mixing layers under supercritical conditions," AIAA J. **40**, 914 (2002).
[18] G. Erlebacher, M. Y. Hussaini, C. G. Speziale, and T. A. Zang, "Toward the large eddy simulation of compressible turbulent flows," J. Fluid Mech. **238**, 155 (1992).
[19] M. S. Graboski and T. E. Daubert, "A modified soave equation of state for phase equilibrium calculation. 1. Hydrocarbon systems," Ind. Eng. Chem. Process Des. Dev. **17**, 443 (1978).
[20] J. F. Ely and H. J. Hanley, "Prediction of transport properties. 1. Viscosity of fluids and mixtures," Ind. Eng. Chem. Fundam. **20**, 323 (1981).
[21] J. F. Ely and H. J. Hanley, "Prediction of transport properties. 2. Thermal conductivity of pure fluids and mixtures," Ind. Eng. Chem. Fundam. **22**, 90 (1983).
[22] J. V. Sengers, R. S. Basu, and J. M. H. Levelt Sengers, "Representative equations for the thermodynamic and transport properties of fluids near the gas–liquid critical point," NASA Contractor Report 3424 (1981).
[23] J. S. Shuen, K. H. Chen, and Y. Choi, "A coupled implicit method for chemical non-equilibrium flows at all speeds," J. Comput. Phys. **106**, 306

(1993).
[24]S. Y. Hsieh and V. Yang, "A preconditioned flux-differencing scheme for chemically reacting flows at all Mach numbers," Int. J. Comput. Fluid Dyn. **8**, 31 (1997).
[25]R. C. Swanson and E. Turkel, "On central difference and upwind schemes," J. Comput. Phys. **101**, 292 (1992).
[26]N. Zong, "Modeling and simulation of cryogenic fluid injection and mixing dynamics under supercritical conditions," Ph.D. dissertation, Department of Mechanical and Nuclear Engineering, Pennsylvania State University, University Park, PA, 2004.
[27]T. Poinsot, and S. Lele, "Boundary conditions for direct simulation of compressible viscous flows," J. Comput. Phys. **101**, 104 (1992).
[28]S. C. Crow and F. H. Champagne, "Orderly structure in jet turbulence," J. Fluid Mech. **48**, 547 (1971).
[29]P. Atsavapranee and M. Gharib, "Structures in stratified plane mixing layers and the effects of cross-shear," J. Fluid Mech. **342**, 53 (1997).
[30]I. A. Hannoun, H. J. S. Fernando, and E. J. List, "Turbulence structure near a sharp density interface," J. Fluid Mech. **189**, 189 (1988).
[31]S. Apte and V. Yang, "Unsteady flow evolution in porous chamber with surface mass injection, part 1: Free oscillation," AIAA J. **39**, 1577 (2001).
[32]A. D. Gilbert, "Spiral structures and spectral in two-dimensional turbulence," J. Fluid Mech. **193**, 475 (1988).
[33]K. C. Schadow and E. Gutmark, "Combustion instability related to vortex shedding in dump combustors and their passive control," Prog. Energy Combust. Sci. **18**, 117 (1992).
[34]M. H. Yu and P. A. Monkewitz, "The effect of nonuniform density on the absolute instability of two-dimensional inertial jets and wakes," Phys. Fluids A **2**, 1175 (1990).
[35]M. C. Soteriou and A. Ghoniem, "Effects of the free-stream density ratio on free and forced spatially developing shear layers," Phys. Fluids **7**, 2036 (1995).
[36]T. Liu,"Temporal and spatial stability of real-fluid mixing layer with density stratification," M.S. dissertation, Department of Mechanical and Nuclear Engineering, Pennsylvania State University, University Park, PA, 2004.
[37]B. Chehroudi, D. Talley, W. Mayer, R. Branam, J. J. Smith, A. Schik, and M. Oschwald, "Understanding injection into high pressure supercritical environments," Fifth International Conference on Liquid Space Propulsion, Chattanooga, TN, 2003.